ADVANCED OPTICAL MATERIALS
www.advopticalmat.de

Luminescence Temperature Quenching in Mn^{2+} Phosphors

*Arnoldus J. van Bunningen, Atul D. Sontakke, Ruben van der Vliet, Vincent G. Spit, and Andries Meijerink**

Narrower band red and green emission in phosphor-converted white light-emitting diodes (wLEDs) can improve the efficacy and color gamut in lighting and display applications. A promising luminescent ion is Mn^{2+} that can have both narrowband green (tetrahedral coordination) and red (octahedral coordination) emission. Unlike in earlier lighting applications of Mn^{2+} phosphors, temperature quenching is important in wLEDs. Insight into the thermal quenching behavior of Mn^{2+} luminescence is lacking. Here systematic research is reported for a variety of Mn^{2+}-doped phosphors; a huge variation in the luminescence quenching temperature T_{50}, ranging from 50 K for Mn^{2+} in ZnTe to 1200 K in $MgAl_2O_4$, is revealed. The value T_{50} shows a positive correlation with the bandgap of the host, but no correlation with the full width half maximum (FWHM) of the emission band, indicating that thermally activated photoionization, not thermal crossover, is the operative quenching mechanism. This is confirmed by thermally stimulated luminescence (TSL) measurements that show a rise in TSL signal following photoexcitation at temperatures around T_{50} providing evidence that quenching is correlated with generation of free charge carriers. Based on these findings, as a design rule is obtained that for temperature-stable Mn^{2+} luminescence in (high power) LEDs a wide-bandgap host material is required.

1. Introduction

Light-emitting diodes (LEDs) have been a revolution in the lighting industry. Since the discovery of the blue (In,Ga)N chip, LED-based technology is rapidly taking over the lighting industry. LED-based lighting has a superior efficiency and lifespan compared to incandescent and fluorescent lighting. Most lighting applications rely on phosphor-converted LED (pcLED). In pcLEDs, a luminescent material (phosphor) is combined with a blue chip to convert part of the blue light to green, yellow, and/or red light. The combination of the blue light with the phosphor-converted light is perceived as white light. By varying the composition of the phosphor mix, any desired spectral distribution can be obtained to meet the needs of specific applications. For example, for indoor housing applications, there is a demand for warmer white light, requiring a stronger red component. In spite of the wide range of available phosphor materials, there is a still need of better materials to convert blue light into narrowband red and green emission. Presently used red LED phosphors have a spectrum that extends into the deep red/near infrared (NIR) region where the eye sensitivity is lower thus reducing the lumen/*W* efficacy. Narrowband red phosphors can mitigate this problem. Narrowband green phosphors are especially advantageous for display applications to improve filter transmission efficiency and extend the color gamut. In the last decade, several new commercially interesting narrowband emitters have been discovered. For example, β-SiAlON:Eu^{2+} emitting in the green around 535 nm with a full width half maximum (FWHM) of 55 nm is suitable for display and lighting applications. Very popular for displays is the red narrow line emission around 630 nm of K_2SiF_6:Mn^{4+} (KSF), but it has issues for high power lighting (fast saturation and low stability).[1] For indoor lighting, $Sr[LiAl_3N_4]$:Eu^{2+} (SLA) is a good red component emitting at 650 with an FWHM of 50 nm.[2]

A promising activator ion for narrowband red and green emission is Mn^{2+}. Mn^{2+} luminescence has been used extensively in the past in lighting and display applications. It has a tuneable emission wavelength ranging from green to the near infrared (500–700 nm) depending on the type of ligand and coordination symmetry. Typically, Mn^{2+} emits in the green in tetrahedral coordination and in the red in octahedral coordination. Additional tuning is possible through covalency to redshift the emission to longer wavelengths for more covalent ligands/host lattices through the nephelauxetic effect. Early applications involve willemite Zn_2SiO_4:Mn^{2+}, a famous green emitting material named after the Dutch King William, that has been applied in displays and fluorescent tubes.[3] The most widely used phosphor in early fluorescent tubes was the halophosphate $Ca_5(PO_4)_3X$:Sb^{3+}, Mn^{2+} (X = F and Cl) discovered in 1942 by McKeag et al.[4,5] It replaced the highly toxic $(Zn,Be)_2SiO_4$:Mn^{2+}

A. J. van Bunningen, A. D. Sontakke, R. van der Vliet, V. G. Spit, A. Meijerink
Debye Institute for Nanomaterials Science
Utrecht University
Utrecht 3584 CC, The Netherlands
E-mail: A.meijerink@uu.nl

The ORCID identification number(s) for the author(s) of this article can be found under https://doi.org/10.1002/adom.202202794.

DOI: 10.1002/adom.202202794

phosphor in white light fluorescent tubes and is still used in inexpensive fluorescent tubes. By adjusting the Sb^{3+}:Mn^{2+} ratio, the color temperature could easily be adjusted by varying the contribution of blue Sb^{3+} and orange Mn^{2+} emission. ZnS:Mn^{2+} has been widely applied in electroluminescent displays. A more recent example of an efficient and narrowband green phosphor with Mn^{2+} is $BaMg_2Al_{16}O_{27}$:Eu^{2+}, Mn^{2+} that was used in fluorescent tubes.

In the various applications of Mn^{2+} emission, the excitation involved high-energy UV photons or fast electrons. For application in white LED (wLED) excitation in the near UV or blue spectral region is required. This poses a problem for Mn^{2+}. The d–d transitions in the visible and near-UV regions for Mn^{2+} are both parity- and spin-forbidden, resulting in extremely low absorption coefficients for these transitions. A possible solution is sensitization with, for example, Eu^{2+} or Ce^{3+}, relying on energy transfer to Mn^{2+}. This requires close proximity of Mn^{2+} and the sensitizer ion.[6,7]

In addition to the sensitization issues, thermal quenching may pose a problem for Mn^{2+} phosphors in LED application where the temperature around the chip can reach up to 150 °C, much higher than in earlier applications of Mn^{2+} phosphors mentioned above. At elevated temperatures, phosphors show thermal quenching of the luminescence. Most commercially used phosphors in LEDs have Ce^{3+}, Eu^{2+}, or Mn^{4+} incorporated. For these ions, the luminescence quenching mechanism has been widely studied and is well understood. The ^2E emission from Mn^{4+} quenches via thermal crossover (TC) via the $^4T_2$ excited state.[8] Ce^{3+} and Eu^{2+} often quench via thermally assisted photoionization (PI).[8–10] Surprisingly, research on thermal quenching of Mn^{2+} has been very limited, and the thermal quenching mechanism of Mn^{2+} emission has gained little attention and is therefore still poorly understood. For future applications of Mn^{2+} phosphors in wLEDs insight in the thermal quenching behavior of Mn^{2+} is crucial. A few articles mention the thermal quenching and/or a quenching mechanism but lack systematic measurements to provide evidence for the suggested quenching mechanism. Both thermally activated photoionization[11] and TC[12] have been suggested but no evidence for either mechanism is provided. In phosphors where Mn^{2+} emission is sensitized, for example, by Ce^{3+} or Eu^{2+}, the quenching temperature of the sensitizer is important as well. If the sensitizer has a lower quenching temperature than Mn^{2+} the quenching of the sensitizer will be the dominant and determine thermal quenching behavior of the Mn^{2+} phosphor.

The two possible quenching mechanisms for Mn^{2+} are thermal crossover and thermally assisted photoionization and are depicted in **Figure 1**. For TC thermal excitation to a higher vibrational level in the excited state can induce crossover to the ground state. For Mn^{2+} this involves a high vibrational level of the $^4T_1$ excited state, which overlaps with a very high vibrational level of the $^6A_1$ ground state. The probability for crossover scales with the overlap of the vibrational wavefunctions, which increases as higher vibrational levels are thermally occupied (see Figure 1). Following crossover, the system will relax nonradiatively down the ladder of vibrational energy levels in the ground state. Thermally activated photoionization occurs when Mn^{2+} is in the $^4T_1$ excited state, and thermal energy is sufficient to promote an electron from the excited state to the conduction band. The electron in the conduction band (CB) has an increased mobility and will be trapped at impurity or defect sites in the material that function as "killer sites" that facilitate nonradiative emission. The mechanism of temperature quenching by thermally activated photoionization has

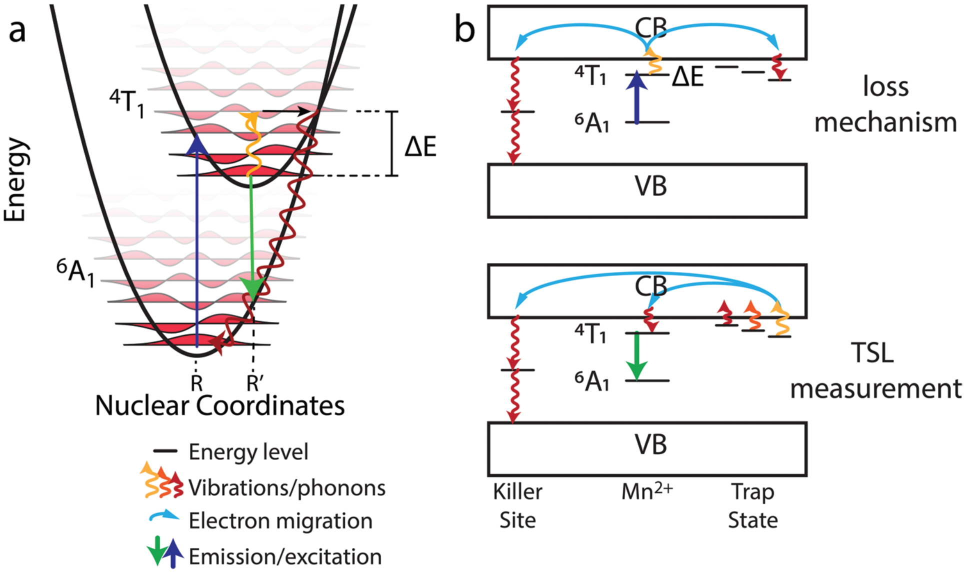

Figure 1. Potential quenching mechanisms for Mn^{2+} emission. a) Diagram of thermal crossover (TC). After Mn^{2+} is excited to the $^4T_1$ level at elevated temperatures higher vibrational levels are populated. Overlap with a very high vibrational level of the ground state allows crossover followed by nonradiative relaxation to the zero-vibrational level of the ground state. b) Diagram of thermally assisted photoionization (PI). Thermal excitation of an electron from the $^4T_1$ excited state to the conduction band results in luminescence quenching. Thermally stimulated luminescence (TSL) can be used as a probe for PI. In case of PI, part of the thermally released electrons can be trapped, leaving behind Mn^{3+}. Heating the sample in the dark causes trap states to thermally empty and part of the electrons will recombine with Mn^{3+} resulting in Mn^{2+} in the excited $^4T_1$ state and Mn^{2+} emission.

been widely investigated and clearly established in Eu^{2+}- and Ce^{3+}-doped phosphors.[9,10] Still, the details on the quenching mechanism following ionization of the electron to the conduction band and the nature of the quenching centers remain unknown, and identification of defects and impurities that play a role in luminescence quenching in phosphors remains one of the great challenges in the field.

In this paper, we systematically investigate the thermal quenching of Mn^{2+} luminescence in a variety of host lattices. The luminescence properties are measured over a wide temperature range, up to temperatures as high as 1200 K. We observe that the quenching temperatures of the Mn^{2+} emission vary strongly from 50 K up to a record high 1190 K. To determine the mechanism for thermal quenching, thermally stimulated luminescence (TSL) measurements were done for Mn^{2+} in a selection of host materials. It was concluded that the dominant quenching mechanism of the Mn^{2+} emission is thermally assisted photoionization. Further research into the correlation of the quenching temperature with either the bandgap of the host (indicating PI) or the full width at half maximum (FWHM) of the emission band (indicating TC) shows a clear correlation with the bandgap but not the FWHM, which confirms that thermally activated photoionization is the universal quenching mechanism for Mn^{2+} luminescence. This is consistent with the narrow bandwidth of Mn^{2+} emission reflecting a small off-set between ground- and excited-state parabolas, which results in a high activation barrier for thermal crossover.

2. Experimental Section

Two classes of materials were synthesized via typical solids state synthesis methods (see Table S1 in the Supporting Information for specific synthesis conditions). In the first group of host lattices, the Mn^{2+} ion occupies a well-defined tetrahedral site. In the second group, Mn^{2+} occupies one or more (close to) octahedral sites. The first group contains AlN, $Ba_2MgSi_2O_7$, $MgAl_2O_4$, $MgGa_2O_4$, Na_2MgGeO_4, $ZnAl_2O_4$, $ZnGa_2O_4$, Zn_2SiO_4, Zn(S,Se) (wurtzite), and ZnS-zb (zincblende). The second group of Mn^{2+}-doped materials includes $Ba_3MgSi_2O_8$, $Ba_2Ca(BO_3)_2$, $Ba_2Mg(BO_3)_2$, $Ca_3MgSi_2O_8$, α-$Ca_3(PO_4)_2$, β-$Ca_3(PO_4)_2$, $CaSiO_3$-pwo (pseudo wollastostonite), $CaSiO_3$-wo (wollastonite), $LiScSi_2O_6$, and $Sr_3MgSi_2O_8$. To check phase purity of the synthesis products a Philips X-ray diffractometer was used. The $K\alpha$ radiation of Cu was used ($\lambda = 1.5401$ Å). The machine was operated at 40 kV and 20 mA current.

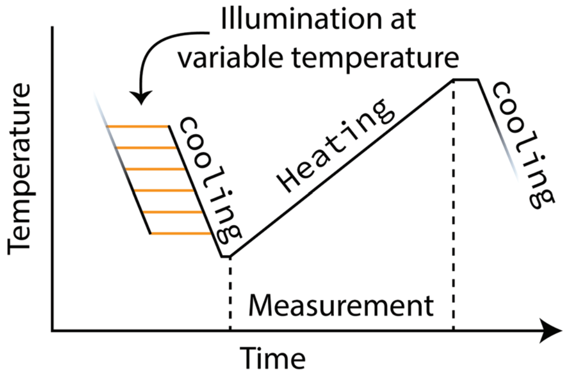

Figure 2. Schematic diagram of the temperature profile for the temperature-dependent TSL measurements. The samples were illuminated at various temperatures for 5–20 min. After the lamp was turned off, the sample was rapidly cooled and a thermally stimulated luminescence curve was recorded.

All spectroscopic measurements were done using an Edinburgh Instruments FLS 920 spectrofluorometer. As an excitation source, a 450 W xenon lamp was used for recording excitation and emission spectra. Alternatively, for luminescence decay measurements, an Opetek Opolette HE355L tunable laser was used, with a variable repetition rate between 1 and 20 Hz and ≈10 ns pulse width. For photoluminescence (PL) and photoluminescence excitation (PLE) spectra and most decay curve measurements, an R928 Hamamatsu PMT was used as a detector. For other decay curves, an H74220 Hamamatsu PMT was used. For the time-resolved measurements the signal of the detector was recorded with a Pico Quant Timeharp 260 card. For temperature-dependent measurement as well as TSL measurements, a Linkam THMS600 was used with a temperature range from −190 to 600 °C. Some materials were measured up to even higher temperatures with a Linkam TS1000, with a temperature limit of 1000 °C.

As discussed above, the process that is responsible for PI quenching can also fill traps giving rise to a TSL signal upon heating in the dark. If PI is the luminescence quenching mechanism, filling of traps should occur in the same temperature region where temperature quenching of the luminescence was observed. In **Figure 2**, the strategy to unravel the quenching mechanism through TSL measurements is shown and is similar to the approach pioneered by Ueda et al. for $Y_3Al_5O_{12}$:Ce.[10] Prior to the TSL experiment, the sample was illuminated at variable temperatures. The wavelength of the illuminating light was chosen to be at long wavelengths, exciting Mn^{2+} into a low excited state to ensure that no direct escape from a high excited (charge transfer, CT) state can occur. Typically, this means exciting with wavelengths longer than 420 nm. Excitation in a high-energy CT state can give rise to direct escape to the conduction band, competing with relaxation to the emitting $^4T_1$ state resulting in ionization (and a TSL response) unrelated to thermal quenching. For excitation in a low-energy $3d^5$ state well below the conduction band, fast relaxation to the emitting state occurs. Now, the illumination temperature will determine the probability to be thermally excited from the $^4T_1$ state to the conduction band and a subsequent observation of TSL serves as a signature for PI luminescence quenching.

It was important that after illumination at elevated temperatures, the sample was cooled rapidly to limit detrapping. Once the sample was cooled, the sample was gradually heated in the dark and the thermally stimulated Mn^{2+} emission was recorded. This TSL signal originated from the emptying of the traps. Thermally excited electrons in the CB can recombine with Mn^{3+} and give rise to the Mn^{2+} ions in the $^4T_1$ excited state and Mn^{2+} emission. The more traps that were initially filled during the illumination stage, the higher the TSL signal detected during the heating step will be. This allows probing of thermally activated photoionization at different illumination temperatures to check if there is a correlation between thermal quenching of the Mn^{2+} emission and photoionization.

The samples were excited for 5–20 min (depending on the host material) with a wavelength corresponding to a d–d transition of the Mn^{2+} ion (no wavelengths shorter than 420 nm were used). The excitation was done while the sample was kept at various fixed temperatures. After the sample was excited at elevated temperature, it was rapidly cooled down before the TSL measurement started. The samples were then heated in the dark (no illumination/excitation) and the Mn^{2+} luminescence was measured as a function of temperature.

3. Results and Discussion

To elucidate the temperature quenching mechanism of Mn^{2+} emission, a wide variety of host lattices were investigated to vary covalency, local coordination symmetry, and bandgap. Temperature-dependent properties of the Mn^{2+} luminescence were studied in AlN, $Ba_2MgSi_2O_7$, $Ba_3MgSi_2O_8$, $Ba_2Ca(BO_3)_2$, $Ba_2Mg(BO_3)_2$, $Ca_3MgSi_2O_8$, α-$Ca_3(PO_4)_2$, β-$Ca_3(PO_4)_2$, $CaSiO_3$-pwo (pseudo wollastostonite), $CaSiO_3$-wo (wollastonite), $LiScSi_2O_6$, $MgAl_2O_4$, $MgGa_2O_4$, $NaMgGeO_4$, $Sr_3MgSi_2O_8$, $ZnAl_2O_4$, $ZnGa_2O_4$, Zn_2SiO_4 Zn(S,Se) (wurtzite), and ZnS-zb (zincblende). For $ZnGa_2O_4$ and AlN doped with Mn^{2+} the luminescence properties will be discussed in more detail. The luminescence spectra and decay curves for Mn^{2+} in the other materials are shown in the Supporting Information.

The emission of Mn^{2+} in tetrahedral coordination in the oxide samples is in the green spectral region, around 510–520 nm, and has a fairly narrow bandwidth with an FWHM of 0.1–0.2 eV. The emission of AlN:Mn^{2+} is around 600 nm and for Zn(S,Se) around 580 nm. All these emission bands correspond to the $^4T_1 \rightarrow {}^6A_1$ transition. The shift in the emission wavelength is mainly caused by the stronger nephelauxetic effect of the more covalent anions (N^{3-}, S^{2-}) coordinating Mn^{2+} in the different host materials while also a higher crystal field splitting for N^{3-} ligands shifts the Mn^{2+} emission to longer wavelengths. The emission of Mn^{2+} in the octahedral coordination in the oxide samples is in the red/deep red spectral region ranging from 600 to 700 nm. The FWHM ranges from 0.3 to 0.6 eV. The shift in the emission wavelength with respect to the tetrahedal symmetry is due to the stronger crystal field strength of Mn^{2+} in octahedral coordination.

3.1. $ZnGa_2O_4$:Mn^{2+}

To investigate the thermal quenching behavior of Mn^{2+}, the temperature-dependent optical properties for Mn^{2+} in $ZnGa_2O_4$ were studied. The emission spectra of $ZnGa_2O_4$:Mn^{2+}, excited with 290 nm light, are shown in **Figure 3**a. At low temperatures (around 100 K), a sharp peak is observed at 500 nm with structured side bands on the longer wavelength side, showing sharp features around 502, 509, and 517 nm. The 500 nm line is assigned to a zero-phonon line and the longer wavelength features to vibronic lines. The presence of individual vibronic lines at low temperature is often observed for Mn^{2+} and is typical for a luminescent ion with limited relaxation in the excited state (small Huang–Rhys factor *S*, indicating a small off-set between the ground- and excited-state equilibrium distances, $R - R'$ in Figure 1).[8,10] This small relaxation is directly related to the narrow bandwidth (small FWHM) that is typically observed for Mn^{2+} emission. As the temperature rises the vibronic peaks widen and merge into one broader band that continues to broaden with increasing temperature, as is typically observed for emission bands. The total emission intensity drops gradually with increasing temperature from 100 to 300 K. Between 325 and 400 K, the emission drops rapidly and at 500 K the emission is at only 2% of the maximum intensity. The intensity

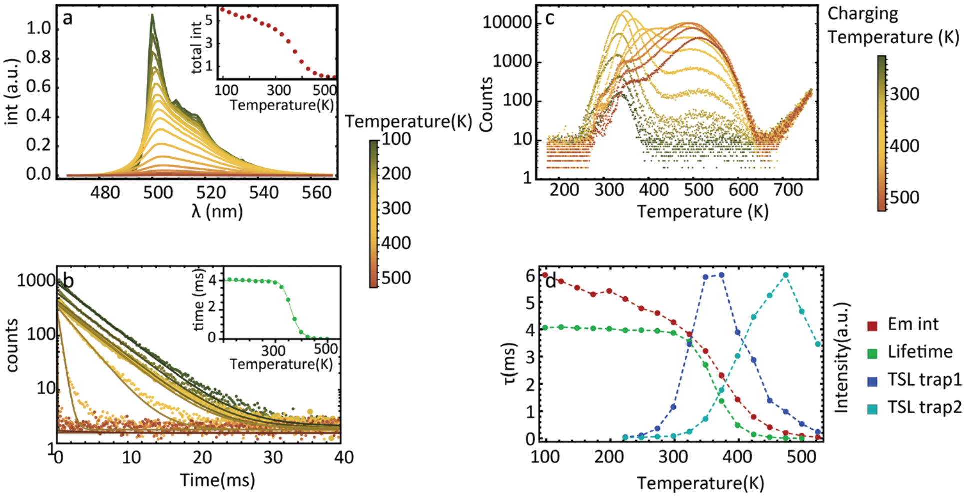

Figure 3. Temperature-dependent luminescence properties of $ZnGa_2O_4$:1%Mn. a) Emission spectra and intensity (inset) at various temperatures for excitation at 290 nm. b) Luminescence decay curves and decay times (inset) at various temperatures for pulsed excitation at 450 nm and observing the emission at 520 nm. c) TSL curves after the sample was excited with 450 nm for 5 min at different temperatures, followed by cooling to 300 K. The TSL was subsequently monitored. d) The three figures in panels (a)-(c) are combined in a single graph to show the relation between the drop in emission lifetime, drop in emission intensity, and increase of the TSL signal in the temperature range where the Mn^{2+} emission is quenched between 320 and 420 K.

of the emission is proportional to the quantum yield (ratio of radiative decay rate and total decay rate) and can be described by

$$I(T) \propto \frac{P_r(T)}{P_r(T) + P_{nr}(T)} \tag{1}$$

Here P_r and P_{nr} are the probability of radiative and nonradiative decay as a function of T. The thermal quanching temperature T_{50} is defined as the temperature at which $P_r = P_{nr}$ and thus the intensity is at 50% of its low temperature value $I(0)$. When we assume that P_r is constant as a function of temperature (which we will see in the following sections is not always the case) and that P_{nr} as a function of temperature can be aproximated by the Arrhenius equation we obtain

$$I(T) = \frac{I(0)}{1 + A * e^{-\Delta E/kT}} \tag{2}$$

where ΔE is an activation barrier for nonradiative decay and A is a constant prefactor. Measuring emission intensity as a function of temperature to probe thermal quenching can show variations in intensity that are not related to thermal quenching, for example, when the oscillator strength of the absorption transition is temperature dependent or when spectral broadening or shift of the absorption line reduces absorption at the excitation wavelength. This gives rise to intensity variations that are not related to thermal quenching.[8,12] In addition to fundamental problems also trivial aspects such as changes in alignment, collection efficiency, or excitation source intensity can give rise to intensity variations. The decrease in intensity observed between 100 and 300 K for $ZnGa_2O_4$:Mn^{2+} is probably related to these types of effects. A fast and reliable method to determine T_{50} is measuring the emission lifetime as a function of temperature. As nonradiative decay sets in, the emission lifetime shortens. To determine the lifetime, the luminescence decay curves are fitted with a single exponential function. The observed emission decay time τ is dependent on the radiative rate P_r as well as the nonradiative rate P_{nr}

$$\tau(T) = \frac{1}{P_r(T) + P_{nr}(T)} \tag{3}$$

Comparison of Equations (3) and (1) reveals that they have the same denominator (sum of radiative and nonradiative decay rates), which shows that $I(T)$ and $\tau(T)$ vary in the same way with temperature, if the radiative decay rate is temperature independent: $I(T) \propto \tau(T)$. When thermally activated nonradiative decay sets in, both the luminescence intensity and decay time decrease proportional to the quantum yield. For Mn^{2+} luminescence (and also other luminescent ions) often temperature-dependent decay measurements give a more reliable determination of the quenching temperature as intensity fluctuations related to other causes (e.g., change in absorption strength and alignment) can affect intensity but not the luminescence decay.

To probe the thermal quenching temperature of the Mn^{2+} emission in $ZnGa_2O_4$ additionally temperature dependent life time measurements were done. Figure 3b shows the luminescence decay curves of the Mn^{2+} emission as a function of temperature, while excited with a 420 nm laser, and monitored at 520 nm. The decay curves are largely single exponential with a faster initial decay (approximately first milliseconds). This faster decay is ascribed to emission from Mn^{2+} nearby a quenching center and energy transfer to the quenching sites results in a faster decay. In the single exponential fitting procedures, this faster initial decay is not considered and single exponential fits starting after 1 ms results in the temperature-dependent decay times that are plotted in the inset of Figure 3b. Between 100 and 300 K, the lifetime remains constant at 4 ms and above 325 K it starts to drop, very similar to the temperature region where the fast drop in emission intensity is observed. Similar to the Arrhenius behavior of the emission intensity, the change of the lifetime as a function of temperature can be described by the following equation[4]

$$\tau(T) = \frac{\tau_r(T)}{1 + A * e^{-\Delta E/kT}} \tag{4}$$

where $\tau_r(T)$ is the raditiave life time at temperature T ($\tau_r(T) = 1/P_r(T)$). By fitting the measured lifetime to this equation, it was possible to determine the T_{50} at 360 K for $ZnGa_2O_4$:Mn^{2+}, very similar to the 375 K determined from the temperature-dependent intensity measurements.

The results discussed above show that the quenching temperature can be determined accurately and consistently, but it does not give information on the quenching mechanism. For both quenching mechanisms (PI and TC), Arrhenius-type behavior is expected. In the case of TC the energy barrier (ΔE) is often considered as the energy difference between the zero-vibrational state of the excited $^4T_1$ level and the crossover point between the $^6A_1$ and $^4T_1$ parabolas.[13] For PI ΔE is the energy gap from the $^4T_1$ to the CB.[9] To distinguish between the two quenching mechanisms, PI or TC, TSL measurements can help. As outlined above, in this procedure TSL is measured following long wavelength excitation at various temperatures. In the case of $ZnGa_2O_4$:Mn^{2+}, the sample was illuminated with 450 nm for 5 min. The results for $ZnGa_2O_4$:Mn^{2+} are shown in Figure 3c. When a TSL signal is observed, this indicates that electrons have been released during photoexcitation of Mn^{2+} and are subsequently trapped. The TSL peaks at certain temperatures reflect the trap depth for the trapped electrons where deeper traps give rise to a TSL peak with a maximum at higher temperatures. For $ZnGa_2O_4$:Mn^{2+} the TSL curves show at least two distinct traps, one corresponding to the TSL peak around 320 K and one around 500 K. At even higher temperatures, above ≈650 K, the TSL curves show a rise which is caused by blackbody radiation. When comparing the TSL curves recorded after different charging temperatures it can be seen that the peak at 320 K increases steadily until a charging temperature of 350/370 K. This coincides with the temperature region where thermal quenching of the Mn^{2+} emission is observed. At even higher temperatures, the TSL peak intensity declines but remains visible even at the highest charging temperatures. The peak at 500 K shows a similar trend and rises starting at 320 K until a charging temperature of 450 K after which it declines. The integrated intensities of the peaks at 350 and 500 K are shown in Figure 3d as "TSL trap1" and "TSL trap2," respectively. The rise of both peaks is attributed to an increase of traps filled due to thermal ionization of the Mn^{2+}. At elevated temperature, the detrapping rate starts to compete with the trapping rate and the signal drops, first for the shallower TSL trap1 and then for the deeper TSL trap2.

The two traps correspond to different defects in the structure. The peak at 300 K is well known for persistence in $ZnGa_2O_4$:Cr^{3+} but has also been observed for $ZnGa_2O_4$:Ni^{2+}. The peak here is caused by an antisite pair defect, Zn'_{Ga} and $Ga^{\cdot}_{Zn}$ capturing an electron and hole, forming $Zn^{\times}_{Ga}$ and $Ga^{\times}_{Zn}$. These electron and hole will be released around 300 K.[14,15] The peak at 500 K is not observed in $ZnGa_2O_4$:Cr^3.[16] Our samples do not include Cr, but are doped with Mn instead. This would indicate that the trap at 500 K is either induced or created by the incorporation of Mn.

Figure 3d shows a combined picture of the temperature-dependent luminescence properties of $ZnGa_2O_4$:Mn^{2+}. In red the total emission, in green the luminescence lifetime and in dark and light blue the integrated signal for the two peaks in the TSL curves are shown as a function of illumination temperature. The total emission and TSL intensity were normalized to allow for better comparison with the lifetime. The coincidence between the temperature region where thermal quenching of the Mn^{2+} emission observed (drop in intensity and decrease luminescence life time) and the filling of traps provide evidence that thermally activated photoionization is responsible for the thermal quenching of the Mn^{2+} emission in $ZnGa_2O_4$.

3.2. AlN:Mn^{2+}, Zn_2SiO_4:Mn^{2+}, and $MgGa_2O_4$:Mn^{2+}

Next to $ZnGa_2O_4$:Mn^{2+} temperature-dependent emission, lifetime, and TSL measurements were done for AlN:Mn^{2+}, Zn_2SiO_4:Mn^{2+}, and $MgGa_2O_4$:Mn^{2+}. The results for AlN:Mn^{2+} are shown in **Figure 4** while for Zn_2SiO_4:Mn^{2+} and $MgGa_2O_4$:Mn^{2+} the experimental data can be found in Figures S13 and S17 (Supporting Information), and only the combined plots of temperature dependence of intensity, luminescence life time, and TSL signal are shown. The temperature-dependent emission of AlN:Mn^{2+} is shown in Figure 4a for a wide temperature range, from room temperature (RT) up to 1123 K. The Mn^{2+} emission is centered around 610 nm and slowly widens with increasing temperature. Around 700 K a rapid drop in total emission intensity is observed. When the temperature reaches 1000 K strong blackbody radiation appears in the spectrum at longer wavenlength. The temperature-dependent luminescence decay curves for Mn^{2+} in AlN are shown in Figure 4c. The decay time remains constant at 1.2 ms until ≈700 K and then rapidly drops. The T_{50} quenching temperatures as derived from the temperature dependence of the emission intensity and decay times are in good agreement, 852 and 824 K, respectively. In Figure 4b, the TSL curves of the Mn^{2+} emission after 520 nm illumination at different temperatures are shown. All

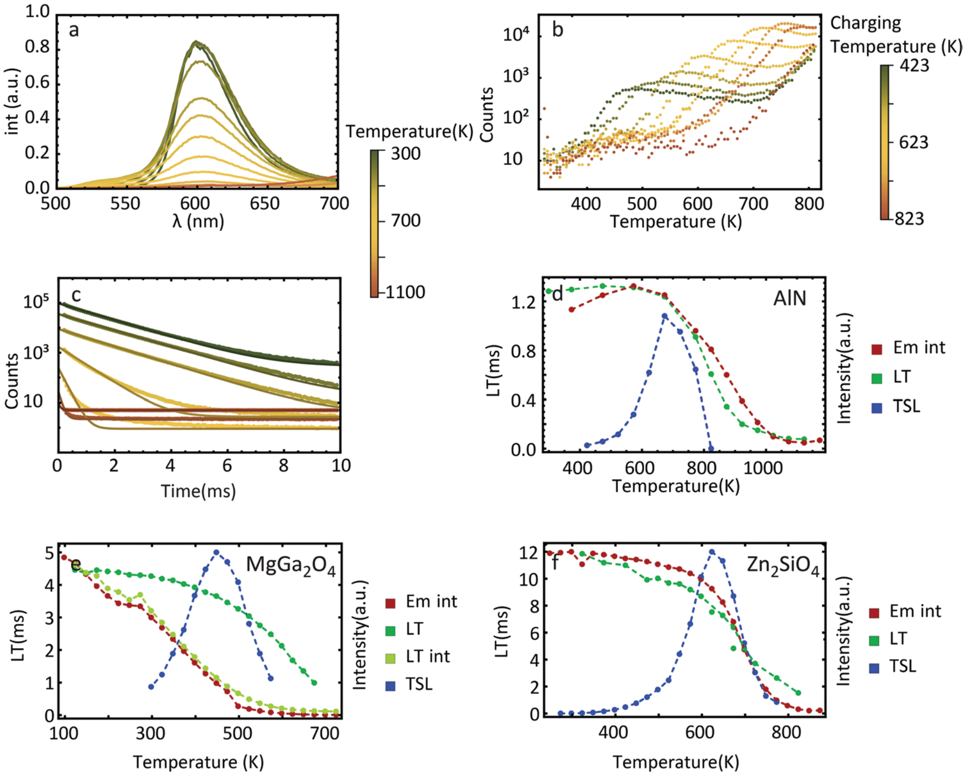

Figure 4. Temperature-dependent luminescence properties of AlN:1%Mn^{2+}, $MgGa_2O_4$:1% Mn^{2+}, and Zn_2SiO_4:1% Mn^{2+}. a) Emission spectra at various temperatures for excitation at 300 nm. b) TSL curves after the sample was excited at 520 nm for 5 min at different temperatures. c) Luminescence decay curves at various temperatures after pulsed excitation at 515 nm for emission at 630 nm. d) The three figures in panels (a)–(c) are combined in a single graph to show the relation between the drop in emission lifetime, emission intensity, and increase of the TSL signal. e) Temperature-dependent luminescence properties of $MgGa_2O_4$:1% Mn^{2+} showing the relation between the drop in emission lifetime, emission intensity, and increase of the TSL signal and (see Figure S13 in the Supporting Information). The light green curve shows the total counts during the lifetime measurements. f) Temperature-dependent properties of Zn_2SiO_4:1% Mn^{2+} showing the relation between the drop in emission lifetime, emission intensity, and increase of the TSL signal (see Figure S17 in the Supporting Information).

TSL curves show a broad TSL band between 400 and 700 K. No distinct peaks are visible which implies the existence of a wide variety of traps. The TSL intensity starts to increase for illumination temperatures above 600 K. The TSL curve continuously shifts to higher temperatures as the charging temperature is increased, consistent with a variety of traps with different trap depths. The shallower traps are thermally emptied during illumination at the higher temperatures. As a result, charging the traps at higher temperatures changes the distribution of filled traps toward deeper traps. This explains the decrease of the TSL signal on the low-temperature side and shift of the maximum to higher temperatures where the deeper traps are emptied. Clear blackbody radiation is observed in the TSL curves. The blackbody background was subtracted to obtain the TSL signal as a function of illumination temperature. These results are plotted together with the temperature-dependent emission intensity and luminescence decay times in Figure 4d. Similar to the results for $ZnGa_2O_4$:Mn^{2+} the rise in TSL signal coincides with the drop in emission intensity and decay time for the Mn^{2+} emission and provides evidence that thermally activated photoionization is responsible for the thermal quenching of the Mn^{2+} emission in AlN:Mn^{2+}.

For Zn_2SiO_4:Mn^{2+} and $MgGa_2O_4$:Mn^{2+} the temperature-dependent emission intensity and lifetime are shown in Figure 4e,f, together with the TSL signal after varying illumination temperatures. Again, the emission intensities and luminescence lifetimes show a sharp drop at elevated temperatures that coincide with the onset for an increase in TSL signal at elevated illumination temperatures.

The results shown in Figure S13 (Supporting Information) for $MgGa_2O_4$:Mn^{2+} show that the emission intensity is dropping gradually while the lifetime is slowly declining between 300 and 700 K, rather than the steeper drop observed for Mn^{2+} emission in AlN and $ZnGa_2O_4$. $MgGa_2O_4$ has a spinel structure but is characterized by substantial disorder, i.e., some Ga^{3+} occupying tetrahedral sites and some Mg^{2+} on octahedral sites.[17] This disorder causes a variation in local surrounding for Mn^{2+} ions as a result can give rise to variations of the energy gap from the $^4T_1$ level to the conduction band. This explains the more gradual change drop in emission intensity. The partial inversion can also explain the discrepancy between temperature dependence of the lifetime (green curve in Figure 4e) and the emission intensity (red curve). Ions that are quenched give less signal and the signal in the decay curves is thus dominated by emission from unquenched ions with longer emission life times. For an alternative comparison we summed the total counts of each life time measurements, divided by the intensity at $t = 0$ to correct for changes in the alignment or fluctuation in the laser power. The temperature dependence of the intensity of the integrated intensity for the luminescence decay curves (light green curve in Figure 4e) now shows very good overlap with the emission intensity.

The temperature dependence of emission intensity, lifetime, and TSL signal for Zn_2SiO_4:Mn^{2+} are shown in Figure 4f. A clear coincidence of the onset temperature for the drop in intensity and lifetime and increase in TSL signal around 500 K is observed. In the temperature region where quenching occurs, the luminescence decay curves show some afterglow and this complicates the analysis of the decay curves and gives rise to an extra multiexponential component in the decay curves (see Figure S17 in the Supporting Information). This afterglow is ascribed to traps that are filled as a result of thermally activated photoionization at temperatures above 500 K, but there are also shallow traps that empty on a millisecond time scale above 500 K. In general, it has to be realized that the TSL-based method described to identify PI as quenching mechanism relies on the presence of traps with a suitable trap depth; the traps should be deep enough to be stable at the illumination/charging temperature but not so deep that heating to high temperatures with (too) strong blackbody radiation is required or require such high temperatures that the re-ionization of Mn^{2+} cannot compete with emission. The dominant traps in Zn_2SiO_4:Mn^{2+} are relatively shallow, similar to TSL trap 1 in $ZnGa_2O_4$:Mn^{2+}.

In addition to the extensive characterization for the four host lattices discussed above, temperature-dependent emission as well as luminescence lifetime measurements was performed for a variety of other Mn^{2+}-doped materials. The results can be found in Figures S3–S20 (Supporting Information). T_{50} values were determined for Mn^{2+} emission in $Ba_2MgSi_2O_7$, $MgAl_2O_4$, $NaMgGeO_4$, $ZnAl_2O_4$, ZnS (both zincblende and wurtzite), Zn(S,Se) solid solutions, and ZnSe. In all these materials, Mn^{2+} typically occupies well-defined tetrahedral sites. The T_{50} of Mn^{2+} in octahedral sites was also determined in $Ba_3MgSi_2O_8$, $Ba_2Ca(BO_3)_2$, $Ba_2Mg(BO_3)_2$, $Ca_3MgSi_2O_8$, α-$Ca_3(PO_4)_2$, β-$Ca_3(PO_4)_2$, $CaSiO_3$-pwo (pseudo wollastostonite), $CaSiO_3$-wo (wollastonite), $LiScSi_2O_6$, and $Sr_3MgSi_2O_8$. Here Mn^{2+} occupies one or more octahedral sites. For most materials, the T_{50} could be determined by decay measurements.

As discussed above, the more reliable T_{50} values are obtained from temperature-dependent lifetime measurements. Typically, the T_{50} can be found by determining at what temperature the lifetime of Mn^{2+} is half of the lifetime at low temperatures. This is however only correct if the radiative rate of Mn^{2+} is independent of temperature. This is not always the case, especially when Mn^{2+} is located in a highly symmetry environment (inversion symmetry).[18] The parity selection rule is more strict for d–d transitions in inversion symmetry as a prominent mechanism to relax the parity selection rule is admixture of opposite parity states by odd-parity crystal field components. These are absent in inversion symmetry. Coupling with odd-parity (ungerade symmetry) vibrations serves now as a main mechanism to relax the selection rule as is evidenced by strong vibronic lines and a weak zero-phonon line in the emission spectrum. Thermal occupation of these vibrational modes enhances this mechanism and thus increases the radiative decay rate. The change in the lifetime due coupling to odd-parity phonons is described by[8,18]

$$\tau_r(T) = \frac{\tau_r(0)}{\coth(h\nu/2kT)} \quad (5)$$

Here "$h\nu$" is the effective odd-parity vibration energy. For Mn^{2+} emission in host lattices with high symmetry coordination, the emission life time is long and correction for the temperature dependence of the radiative life time is needed to find the correct T_{50}. This includes all host lattices where Mn^{2+} is in octahedral coordination. For some tetrahedral coordination hosts, this correction was done as well, specifically, $MgAl_2O_4$, $ZnAl_2O_4$, and Zn_2SiO_4. In all these hosts, the lifetime of the Mn^{2+} emission is longer than 10 ms at room temperature indicating that the local symmetry is high and coupling with odd-parity vibrations can be expected to significantly contribute to the radiative life time.

To test the hypothesis of photoionization as the dominant quenching mechanism, also TSL measurements were attempted for other Mn^{2+}-doped hosts, viz., $Ba_2MgSi_2O_7$, Na_2MgGeO_4, $MgAl_2O_4$, $ZnAl_2O_4$, ZnS wz, and ZnSe. No TSL signal was observed. For $MgAl_2O_4$ and $ZnAl_2O_4$ this is not surprising as the Mn^{2+} emission in these materials is stable up to extremely high temperatures (T_{50} of 1127 and 1190 K, respectively). This means that high temperatures will be necessary to thermally excite the electron from the $^4T_1$ state to the conduction band, deep and stable traps are needed to later verify the occurrence of photoionization. Even if sufficiently deep traps exist, the temperature necessary to empty this trap will cause strong blackbody radiation that obscures a possible TSL signal. As discussed above, a more general requirement is the presence of traps with a trap depth that is high enough to limit detrapping during the illumination step and not so deep that the temperature necessary for thermal release also cause immediate quenching of the Mn^{2+} emission. If no such trap exists in the material, no TSL signal will be measured even when PI is the quenching mechanism.

For thermal ionization to occur, the energy gap between the conduction band and the $^4T_1$ level of Mn^{2+} is crucial and determines the quenching temperature. It can be expected that this energy difference will be larger for wider-bandgap materials. We therefore compared the T_{50} Mn^{2+} in different materials with the bandgap. The materials that are investigated are insulators and have the bandgap typically above 5 eV. Measurements in this range pose challenges for most absorption spectrometers. For AlN, $MgAl_2O_4$, and ZnS, ZnSe, and ZnTe reliable values were found in refs. [19–23]. For solid solutions of wurtzite Zn(S,Se), the bandgap varies between and 2.7 and 3.6 eV.[24] ZnS zincblende has a bandgap of 3.8 eV. ZnTe has a bandgap of 1.98 eV. For AlN there are multiple sources consistently mentioning a bandgap between 6 and 6.3 eV. In $MgAl_2O_4$ the bandgap was determined via synchrotron radiation to be 8.2 eV. For most other materials, a value for the bandgap was found in literature, but was based on absorption measurements. For the materials that lacked any source, the bandgap was determined by the materials' project.[25] The materials' project uses density functional theory (DFT) calculations to determine the bandgap. Calculating the bandgap by DFT often gives a large deviation from the real experimental bandgap. The deviation between the calculated bandgap and the measured bandgap for AlN $MgAl_2O_4$, ZnS, ZnSe, and ZnTe were compared. For this series, reliable experimental values for the bandgap have been reported, and a clear trend is observed showing a factor of 1.6 difference between the experimental (actual) bandgap and the calculated bandgap (see Figure S22 in the Supporting Information). For the materials that lack an experimentally determined bandgap, we multiplied the calculated bandgap by 1.6 to have a better estimate of the actual bandgap of the materials. The bandgaps of the host materials and the T_{50} values for the Mn^{2+} emission are collected in **Tables 1–3** and plotted in **Figure 5**.

Table 1. The quenching temperature of Mn^{2+} in tetrahedral coordination in various host materials together with the bandgap (experimentally observed or calculated) and the full width half maximum of Mn^{2+} emission in these hosts. For the theoretical bandgap, the bandgap was taken as determined by DFT calculations by the materials project (values shown in the parentheses) and this was multiplied by 1.6 (see also text).

Material	Bandgap [eV]	Theoretical bandgap [eV]	T_{50} [K]	FWHM at 298 K [eV]
$MgAl_2O_4$	8.2[21]	8.2 (5.12)	1191	0.153
$ZnAl_2O_4$	7.0[26]	6.16 (3.85)	1126	0.102
AlN	6.12[20]	6.49 (4.05)	824	0.145
Zn_2SiO_4	5.3[27]	4.41 (2.76)	729	0.190
ZnS-wz	3.82[19]	3.32 (2.08)	700	0.200
ZnS-zb	3.74[19]	3.76 (2.35)	661	0.195
Na_2MgGeO_4	–	5.23 (3.27)	463	0.162
Na_2ZnSiO_4	–	5.11 (3.19)	434	0.145
$MgGa_2O_4$	4.9[28]	3.9 (2.44)	400	0.151
$ZnGa_2O_4$	4.6[29]	3.73 (2.33)	360	0.120
ZnSe	2.69[22]	2.58 (1.61)	352	0.198
Zn_2GeO_4	4.51[30]	3.16 (1.97)	330[30]	0.210
$Ba_2MgSi_2O_7$	–	7.15 (4.47)	298[6]	0.207
ZnTe	1.98[23]	1.73 (1.08)	50[31]	–

The results in Figure 5 show a clear trend that with increasing bandgap; the luminescence quenching temperature of the Mn^{2+} increases. There is one outlier: Mn^{2+} in $Ba_2MgSi_2O_7$ where the T_{50} is lower compared to the other host materials with similar bandgaps. This may be due to an error in the bandgap as only the theoretical bandgap is known. Comparison between theoretical bandgaps and experimentally determined bandgaps shows that the theoretical estimate of bandgaps is not always accurate. Overall, the clear correlation between bandgap and T_{50} quenching temperature confirms

Table 2. The quenching temperature of Mn^{2+} in octahedral coordination in various host materials together with the bandgap (experimentally observed or calculated) and the full width half maximum of Mn^{2+} emission in these hosts. For the theoretical bandgap, the bandgap was taken as determined by DFT calculations by the materials project (values shown in the parentheses) and this was multiplied by 1.6 (see also text).

Material	Experimental bandgap [eV]	Theoretical bandgap [eV]	T_{50} [K]	FWHM [eV]
$Ba_3MgSi_2O_8$	–	7.51 (4.69)	997	0.484
α-$Ca_3(PO_4)_2$	–	8.32 (5.20)	982	0.543[a)]
β-$Ca_3(PO_4)_2$	6.4[32]	8.77 (5.48)	971	0.478[a)]
Sr_3MgSiO_8	5.4[33]	7.5 (4.69)	925	0.339
$CaSiO_3$-pwo	–	7.89 (4.93)	922	0.439[a)]
$LiScSi_2O_6$	–	7.89 (4.93)	921	0.506
$Ba_2Mg(BO_3)_2$	5.7[34]	7.26 (4.54)	907	0.370
$CaSiO_3$-wo	5.5[35]	7.57 (4.73)	800	0.547[a)]
$Ba_2Ca(BO_3)_2$	6.0[34]	6.53 (4.08)	782	0.383
$Ca_3MgSi_2O_8$	5.1[36]	6.12 (3.82)	642	0.329

[a)] Emission from multiple different Mn^{2+} sites is possible.

Table 3. Quenching temperature of Mn^{2+} emission for cubic 8-coordination in two fluorides together with the bandgap (experimentally observed and calculated) and the full width half maximum of Mn^{2+} emission. For the theoretical bandgap, the bandgap was taken as determined by DFT calculations by the materials project (values shown in the parentheses) and this was multiplied by 1.6 (see also text).

Material	Experimental bandgap [eV]	Theoretical bandgap [eV]	T_{50} [K]
CaF_2	11.1[37]	11.6 (7.25)	580[38]
CdF_2	8.4[39]	4.91 (3.07)	338[38]

that PI is the dominant quenching mechanism for Mn^{2+} both in tetrahedral and octahedral coordinations. It is important to realize that deviations from the expected correlation between bandgap and T_{50} can be expected as it is not only the absolute value of the bandgap, but also the position of the Mn^{2+} ground state in the gap (relative to the conduction band) that determines the activation barrier for photoionization. This can explain also some deviations from the expected trend, for example, for the fluorides where the low energy of the F(2p) valence band contributes to the large bandgap. Similarly, the higher T_{50} values than expected based on the bandgap for Mn^{2+} in ZnS, ZnSe, and ZnTe may be explained by a higher energy position of the valence band. For the two modifications of ZnS and the solid solutions Zn(S,Se), a clear correlation is found between bandgap and T_{50} (see Figures S18–S21 and Table S2 in the Supporting Information).

Despite some deviations, the results in Figure 5 clearly show a consistent trend of increasing T_{50} for higher bandgaps for oxides, fluorides, and chalcogenides. For the smaller-bandgap oxides (gallates and germanates), this leads to undesired quenching at the operating temperature of high power LEDs of around 150 °C but in most oxides the quenching temperature is sufficiently high for application in wLEDs. If for specific applications higher thermal stability of the luminescence is required, wider bandgap oxides are needed.

It is also interesting to relate the width of the Mn^{2+} emission bands to the luminescence quenching temperatures. For the thermal crossover mechanism a clear correlation is expected. A larger offset between ground and excited state parabolas will give rise to a broader emission band and a lower luminescence quenching temperature. For decades, this has been the standard model to explain trends in luminescence quenching temperatures. Limiting expansion (or contraction) in the excited state relative to the ground state in stiff lattices and well-designed coordination was used to raise luminescence quenching temperatures. Only when this model failed to explain low quenching temperatures of, e.g., Eu^{2+} or Ce^{3+} emission in host lattices where the emission band width was narrow, another model of photoionization was found to provide an alternative and frequently occurring quenching mechanism.[9,10,37] To investigate the role of TC quenching, in **Figure 6** the FWHM at RT for the Mn^{2+} emission is plotted versus the T_{50} values. The results show no correlation. This provides further evidence that thermally activated photoionization is the dominant thermal quenching mechanism for Mn^{2+} emission and not TC quenching. The FWHM and Stokes shift of emission bands are both determined by the offset of ground- and excited-state parabolas.[9–11] A larger FWHM and Stokes shift are expected with increasing offset of the ($^4T_1$) excited-state parabola with respect to the ($^6A_1$) ground-state parabola. A larger offset leads to a lower activation barrier ΔE (see Figure 1) and thus a lower quenching temperature. Clearly, no correlation

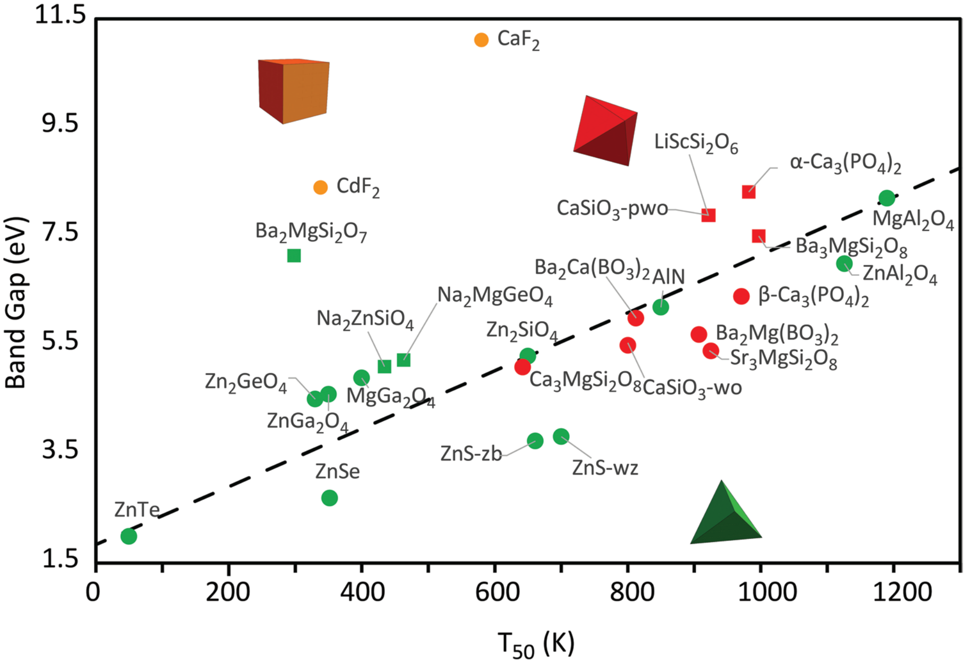

Figure 5. Luminescence quenching temperatures for Mn^{2+} emission in various host lattices versus the bandgap of the host. The red data points are for Mn^{2+} in an octahedral site, green for Mn^{2+} in a tetrahedral site, and orange in a cubic site. The dots indicate experimentally determined bandgaps and squares indicate theoretical bandgaps based on calculations by the materials project[25] (see also text); the dashed lines are added to indicate the trend.

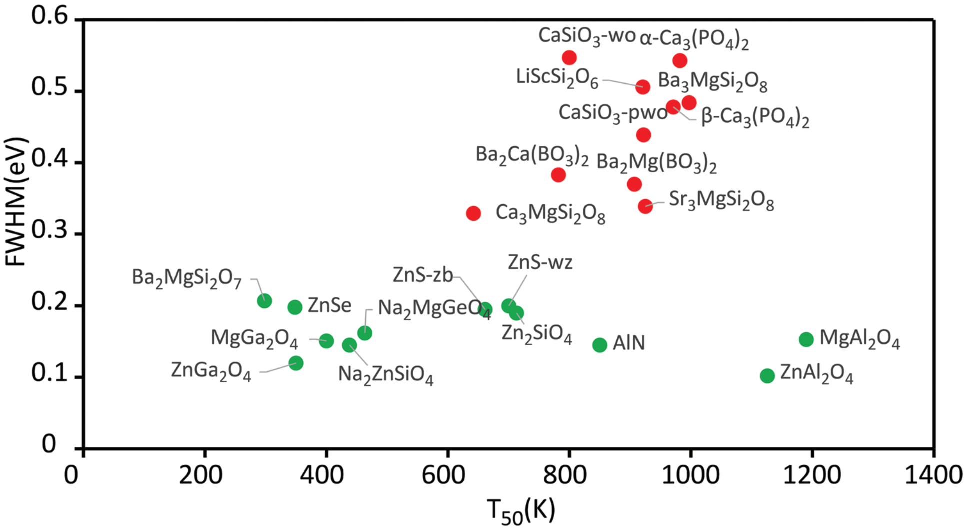

Figure 6. Luminescence quenching temperature of Mn^{2+} emission in various host lattices versus the FWHM of the emission at 300 K of the Mn^{2+} emission in these hosts. Red data points are for Mn^{2+} in an octahedral site, green for Mn^{2+} in a tetrahedral site.

between FWHM and quenching temperature is observed for an extremely wide range of T_{50} values (300–1200 K). This confirms that the dominant quenching mechanism is not thermally activated crossover from the excited state to the ground state. Based on the narrow bandwidth of Mn^{2+} emission this is not unexpected. A narrow bandwidth is indicative of a small relaxation in the excited and a correspondingly high TC quenching temperature. It cannot be excluded that the mechanism for thermal quenching for Mn^{2+} in the two aluminates with T_{50} values above 1000 K is TC although the higher T_{50} (1191 K) is observed for Mn^{2+} emission in the host where the Mn^{2+} emission band has a broader FWHM at 300 K ($MgAl_2O_4$). Three hosts of the octahedrally coordinated Mn can emit from multiple sites (α-$Ca_3(PO_4)_2$, β-$Ca_3(PO_4)_2$, and $CaSiO_3$-wo). This will increase the measured FWHM of the emission of these compounds and therefore for octahedrally coordinated Mn^{2+} TC cannot yet be fully excluded.

Note that the emission FWHM for Mn^{2+} in octahedral coordination is consistently larger than for Mn^{2+} in tetrahedral coordination. The larger FWHM for Mn^{2+} emission in octahedral symmetry can be explained by the steeper slope of the $^4T_1$ excited state line in the $3d^5$ Tanabe Sugano diagram at stronger crystal fields. The much smaller crystal field splitting in tetrahedral coordination compared to octahedral or cubic coordination ($\Delta_T = -4/9\ \Delta_O$; $\Delta_C = -8/9\ \Delta_O$) indicates that tetrahedral Mn^{2+} is in the region where Δ/B is smaller than 10 and where the $^4T_1$ slope is reduced in comparison to the constant, and steep slope in the region with $\Delta/B > 15$.

4. Conclusion

The temperature-dependent luminescence properties of Mn^{2+} have been studied in over 20 host lattices to gain insight into the thermal quenching behavior and mechanism. A huge variation in T_{50} quenching temperatures is observed, from quenching around room temperature ($Ba_2MgSi_2O_7$:Mn^{2+}) or even below room temperature (ZnTe:Mn^{2+}) to record high quenching temperatures around 1200 K ($MgAl_2O_4$:Mn^{2+}). Temperature-dependent emission intensity and lifetime measurements have been related to thermally stimulated luminescence signals after illumination at different temperatures. In four different hosts, the onset temperature for the drop in Mn^{2+} emission intensity and emission life time coincides with illumination temperature at which an onset of TSL signal is recorded. This provides strong evidence for thermally activated photoionization as the dominant quenching mechanism. A clear relation between bandgap of the host materials and the T_{50} quenching temperature confirms that photoionization is responsible for thermal quenching of Mn^{2+} emission. No correlation was found between the emission bandwidth (FWHM) and T_{50}, where a lower T_{50} would be expected for larger bandwidths if the alternative quenching mechanism (thermal crossover from the excited $^4T_1$ to the $^6A_1$ ground states) would be operative. Based on these observations we conclude that luminescence quenching in Mn^{2+}-doped phosphors occurs by thermally activated photoionization and that the thermal quenching behavior can be optimized by choosing wide-bandgap hosts. Still, for most host lattices the thermal quenching temperatures are sufficiently high to prevent thermal quenching in (high power) white LED applications while for specialty applications requiring extremely high thermal quenching can be realized well over 1000 K.

Supporting Information

Supporting Information is available from the Wiley Online Library or from the author.

Conflict of Interest

The authors declare no conflict of interest.

Data Availability Statement

The data that support the findings of this study are available in the supplementary material of this article.

Keywords

luminescence, Mn^{2+}, temperature dependence

Received: November 22, 2022
Revised: December 12, 2022

---

[1] M. A. Van De Haar, M. Tachikirt, A. C. Berends, M. R. Krames, A. Meijerink, F. T. Rabouw, *ACS Photonics* **2021**, *8*, 1784.

[2] L. Gan, Z.-Y. Mao, X.-H. Zeng, Y.-Q. Zhang, Y. Zhao, F.-F. Xu, Y.-C. Zhu, X.-J. Liu, *Mater. Res. Bull.* **2014**, *51*, 205.

[3] Willemite, [online available], https://www.mindat.org/min-4292.html (accessed: August 2022).

[4] A. A. Kaminskii, et al., *Phosphor Handbook*, CRC Press, Boca Raton, FL **2018**.

[5] A. H. McKeag, P. W. Ranby, Improvements in luminescent materials, Great Britain Patent 578,192, filed June 17, 1942; issued June 19, 1946.

[6] A. D. Sontakke, A. J. van Bunningen, F. T. Rabouw, S. Meijers, A. Meijerink, *J. Phys. Chem. C* **2020**, *124*, 13902.

[7] A. D. Sontakke, A. J. Van Bunningen, S. Wakui, A. Meijerink, *Mater. Adv.* **2021**, *2*, 2075.

[8] T. Senden, R. J. A. Van DIjk-Moes, A. Meijerink, *Light: Sci. Appl.* **2018**, *7*, 2047.

[9] P. Dorenbos, *J. Phys.: Condens. Matter* **2005**, *17*, 8103.

[10] J. Ueda, P. Dorenbos, A. J. J. Bos, A. Meijerink, S. Tanabe, *J. Phys. Chem. C* **2015**, *119*, 25003.

[11] S. H. M. Poort, D. Cetin, A. Meijerink, G. Blasse, *J. Electrochem. Soc.* **1997**, *144*, 2179.

[12] D. Böhnisch, J. Rosenboom, A. García-Fuente, W. Urland, T. Jüstel, F. Baur, *J. Mater. Chem. C* **2019**, *7*, 6012.

[13] C. W. Struck, W. H. Fonger, *J. Lumin.* **1975**, *10*, 1.

[14] D. Gourier, A. Bessière, S. K. Sharma, L. Binet, B. Viana, N. Basavaraju, K. R. Priolkar, *J. Phys. Chem. Solids* **2014**, *75*, 826.

[15] V. Castaing, L. Giordano, C. Richard, D. Gourier, M. Allix, B. Viana, *J. Phys. Chem. C* **2021**, *125*, 10110.

[16] S. K. Sharma, A. Bessière, N. Basavaraju, K. R. Priolkar, L. Binet, B. Viana, D. Gourier, *J. Lumin.* **2014**, *155*, 251.

[17] T. Ito, A. Yoshiasa, T. Yamanaka, A. Nakatsuka, H. Maekawa, *Z. Anorg. Allg. Chem.* **2000**, *626*, 42.

[18] A. gen, A. D. Sontakke, S. Wakui, A. Meijerink, *Opt. Mater.* **2022**, *128*, 112433.

[19] O. Brafman, I. T. Steinberger, *Phys. Rev.* **1966**, *143*, 501.

[20] M. E. Levinshtein, S. L. Rumyantsev, M. S. Shur, *Properties of Advanced Semiconductor Materials GaN, AlN, InN, BN, SiC, SiGe*, John Wiley & Sons, Inc., Hoboken, NJ **2001**.

[21] E. Feldbach, I. Kudryavtseva, K. Mizohata, G. Prieditis, J. Räisänen, E. Shablonin, A. Lushchik, *Opt. Mater.* **2019**, *96*, 109308.

[22] S. Adachi, T. Taguchi, *Phys. Rev. B* **1991**, *43*, 9569.

[23] R. E. Dietz, D. G. Thomas, J. J. Hopfield, *Phys. Rev. Lett.* **1962**, *8*, 391.

[24] M. A. Avilés, J. M. Córdoba, M. J. Sayagués, F. J. Gotor, *Inorg. Chem.* **2019**, *58*, 2565.

[25] A. Jain, S. P. Ong, G. Hautier, W. Chen, W. D. Richards, S. Dacek, S. Cholia, D. Gunter, D. Skinner, G. Ceder, K. A. Persson, *APL Mater.* **2013**, *1*, 011002.

[26] R. E. Rojas-Hernandez, F. Rubio-Marcos, I. Romet, A. Del Campo, G. Gorni, I. Hussainova, J. F. Fernandez, V. Nagirnyi, *Inorg. Chem.* **2022**, *61*, 11886.

[27] H. Amekura, K. Kono, N. Kishimoto, C. Buchal, *Nucl. Instrum. Methods Phys. Res., Sect. B* **2006**, *242*, 96.

[28] Z. Galazka, D. Klimm, K. Irmscher, R. Uecker, M. Pietsch, R. Bertram, M. Naumann, M. Albrecht, A. Kwasniewski, R. Schewski, M. Bickermann, *Phys. Status Solidi* **2015**, *212*, 1455.

[29] Z. Galazka, S. Ganschow, R. Schewski, K. Irmscher, D. Klimm, A. Kwasniewski, M. Pietsch, A. Fiedler, I. Schulze-Jonack, M. Albrecht, T. SchröDer, M. Bickermann, *APL Mater.* **2019**, *7*, 022512.

[30] F. Chi, X. Wei, B. Jiang, Y. Chen, C. Duan, M. Yin, *Dalton Trans.* **2018**, *47*, 1303.

[31] L. V. Khoi, J. Kossut, R. R. Galazka, *J. Supercond.* **2003**, *16*, 427.

[32] E. Feldbach, M. Kirm, A. Kotlov, H. Mägi, Luminescence Spectroscopy of Ca-apatites under VUV Excitation. https://photon-science.desy.de/annual_report/files/2010/20101246.pdf (accessed: December 2022).

[33] P. Dewangan, D. P. Bisen, N. Brahme, R. K. Tamrakar, S. Sharma, K. Upadhyay, *Opt. Quantum Electron.* **2018**, *50*, 367.

[34] S. Jayakiruba, S. S. Chandrasekaran, P. Murugan, N. Lakshminarasimhan, *Phys. Chem. Chem. Phys.* **2017**, *19*, 17383.

[35] H. Nagabhushana, B. M. Nagabhushana, M. Madesh Kumar, Chikkahanumantharayappa, K. V. R. Murthy, C. Shivakumara, R. P. S. Chakradharg, *Spectrochim. Acta, Part A* **2011**, *78*, 64.

[36] V. Singh, G. Lakshminarayana, A. Wagh, N. Singh, *Optik* **2020**, *206*, 164240.

[37] T. Tomiki, T. Miyata, *J. Phys. Soc. Jpn.* **1969**, *27*, 658.

[38] P. J. Alonso, R. Alcalá, *J. Lumin.* **1981**, *22*, 321.

[39] C. Raisin, J. M. Berger, S. Robin-Kandare, *J. Phys. C: Solid State Phys.* **1980**, *13*, 1835.